ACS OMEGA

http://pubs.acs.org/journal/acsodf

Article

Heterostructured CeO_2–M (M = Co, Cu, Mn, Fe, Ni) Oxide Nanocatalysts for the Visible-Light Photooxidation of Pinene to Aroma Oxygenates

Mlungisi A. Mavuso, Peter R. Makgwane,* and Suprakas Sinha Ray*

Cite This: *ACS Omega* 2020, 5, 9775–9788

Read Online

ACCESS | Metrics & More | Article Recommendations | Supporting Information

ABSTRACT: Herein, we report the enhanced photocatalytic activity of heterostructured CeO_2 nanocatalysts interfaced with Cu, Co, Ni, Mn, and Fe metal oxides. The CeO_2 catalysts exhibited an enhanced red shift in the visible-light response compared to CeO_2. This improved absorption range effectively suppressed electron (e^-)/hole (^+h) recombination by forming localized energy bands associated with defect oxygen vacancies (V_o) induced by the M^{n+} ions incorporated in CeO_2. Under visible-light irradiation, CeO_2 catalysts are active for α-pinene oxidation to the aroma oxygenates, pinene oxide, verbenol, and verbenone. Both Fe_2O_3–CeO_2 and NiO–CeO_2 gave the highest pinene conversions of 71.3 and 53.1%, respectively, with corresponding pinene oxide selectivities of 57.3 and 58.2%. The enhanced photocatalytic performance of the heterostructured CeO_2 catalysts compared to CeO_2 is attributed to their enhanced visible-light absorption range and efficient suppression of $e^-/^+h$ recombination. The Fe_2O_3–CeO_2 catalyst was highly recyclable and did not show any significant loss of its photoactivity.

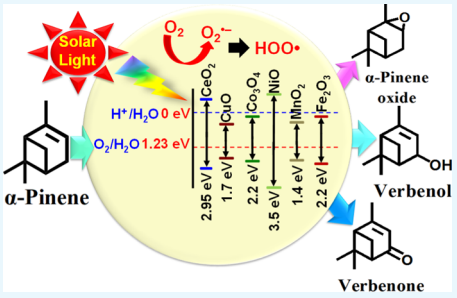

INTRODUCTION

Biomass-derived terpene compounds derived from turpentine oil represent a readily available renewable, inexpensive, and versatile feedstock for the synthesis of key functional performance chemicals for applications in areas such as fragrances, flavors, pharmaceuticals, solvents, and chiral intermediates.[1] One such terpene derivative is α-pinene, whose fraction is more than 60% of the terpene species in turpentine oil. The catalytic oxidation of pinene allows the production of fragrance products including pinene oxide, verbenone, and verbenol, which are isolated as the main constituents of the reaction.[2] Pinene oxide can be isomerized to campholenic aldehyde, an intermediate in the synthesis of sandalwood-like fragrances, such as Sandalore (Givaudan) or Polysantol (Firmenich).[3] Although numerous catalytic systems have been reported for the selective oxidation of pinene, including homogeneous and heterogeneous catalytic systems, the selective oxidation of pinene by heterogeneous catalysts still remains a major challenge.[1,4] For instance, Cao et al.[3] prepared carbon nanotubes for the selective oxidation of pinene using O_2 as an oxidant, and promising results were obtained. However, most of these catalytic systems are limited by the use of extreme reaction conditions, low substrate conversions, and poor selectivity, as well as the use of hazardous solvents, thus rendering pinene catalytic oxidation reactions less efficient and sustainable with respect to green chemistry. Consequently, the quest to design active materials that achieve the efficient and green catalytic conversion of terpenes, particularly pinene oxidation, is an area of ongoing research. The applications of photocatalysis in oxidation reactions for the oxyfunctionalization of the inert C–H bond of several hydrocarbons such as cyclohexane, benzene, and aromatic hydrocarbons are well documented in the literature.[5]

Photocatalysis has evolved over the years into a clean, sustainable, and viable technological process for harvesting and converting solar energy to storable energy or chemical resources.[6] Several different semiconductors have been reported as potential photocatalysts for visible-light photocatalytic organic conversion, including TiO_2, ZnO, Nb_2O_5, and CeO_2.[7,8] Although great progress has been achieved in photocatalytic material design, the development of highly effective visible-light photoactive catalysts for the efficient catalytic oxyfunctionalization of the inert C–H bond, including the typical pinene oxidation reaction, remains elusive. The major factors preventing the application of photocatalysis to selective oxidation reactions include the restricted UV or low visible-light absorption range of these photocatalysts and the generation of uncontrolled nonselective active species (i.e., $^•$OH).[9,10] To control the $^•$OH radicals produced in photocatalytic partial oxidation processes, many photocatalyst

Received: December 20, 2019
Accepted: April 6, 2020
Published: April 23, 2020

https://dx.doi.org/10.1021/acsomega.9b04396
ACS Omega 2020, 5, 9775–9788

modification strategies, such as band-gap modification, selective growth of crystal facets, and surface treatment, have been explored.[10,11] Moreover, band-gap manipulation can extend the light response of photocatalysts to the visible-light region.[12] Band-gap manipulation strategies include doping with transition metals,[13] dye sensitization,[14] and anionic doping.[15] Another important strategy is to couple two or more semiconductor oxides together to generate visible-light active catalysts. Heterojunction semiconductor photocatalysts possess several advantages such as (1) improved charge separation, (2) increased charge carrier lifetimes, and (3) enhanced photocatalytic activities because of the high efficiency of the interfacial charge transfer to the adsorbed substrate. Moreover, the coupling of hybrid catalyst materials results in an increase in the number of available active sites for photochemical reactions.[16,17]

The visible-light response of CeO_2 can be improved by the design of the heterojunction interface with other semiconductors. CeO_2 can only absorb a small portion of the available solar irradiation because it possesses a relatively wide band gap of 2.8−3.2 eV depending on the synthesis method.[18] Heterojunction interface photocatalysts, such as CeO_2/g-C_3N_4,[19] Fe_2O_3/CeO_2,[20] and $BiVO_3/CeO_2$,[17] have been investigated for their activity in photocatalytic oxidation reactions. For instance, Zou et al.[19] developed a hybrid CeO_2/g-C_3N_4 composite as a photocatalyst for the generation of hydrogen under visible-light irradiation.[19] The CeO_2/g-C_3N_4 hybrid composite exhibited superior photocatalytic H_2 evolution under visible-light irradiation. The optimal CeO_2 loading of 5 wt % was found to release higher amounts of H_2 (ca. 4600 μmol/g) when compared to the individual CeO_2 and g-C_3N_4 counterparts. This is due to the enhanced visible-light absorption and faster charge transfer attributed to the stronger interfacial effect caused by hydrogen bonding and p−π hybridization between CeO_2 and g-C_3N_4.[19] Several metal-CeO_2-based nanostructure interface photocatalysts have been designed, including Au/CeO_2, for the oxidation of alcohols and amines,[21] hybrid Au/CeO_2 nanofibers, and a plum-pudding-type Pd@CeO_2 semiconductor for the oxidation of benzyl alcohol.[22] In other studies, electrospun-derived Ag/CeO_2@carbon nanofiber hybrids and Pd/CeO_2 with core−shell and yolk−shell morphologies were designed for the photocatalytic oxidation of benzyl alcohol.[23,24]

In this study, we used the sol−gel method to synthesize heterostructured CeO_2 catalysts with an interface with various nanostructured metal oxides, including Co, Cu, Ni, Mn, and Fe. The effects of the structural interfaces on the photocatalytic activity were evaluated to develop catalysts for the selective photocatalytic oxidation of α-pinene to various aroma oxygenates at room temperature. The heterostructure CeO_2 metal oxide catalysts showed improved photocatalytic oxidation activity compared to the neat CeO_2, and the improvement was dependent on the nature of the base metal oxide interfaced with the CeO_2 semiconductor.

RESULTS AND DISCUSSION

Catalyst Characterization. *Physical and Textural Analyses.* Figure 1 and Table 1 show the N_2 physisorption results of pristine CeO_2 and the heterostructured CeO_2 interfaced metal oxide nanocatalysts. The results are presented as adsorption/desorption isotherms with respective pore size distribution profiles including the Brunauer−Emmett−Teller (BET) surface areas, pore volumes, and diameters. The pristine

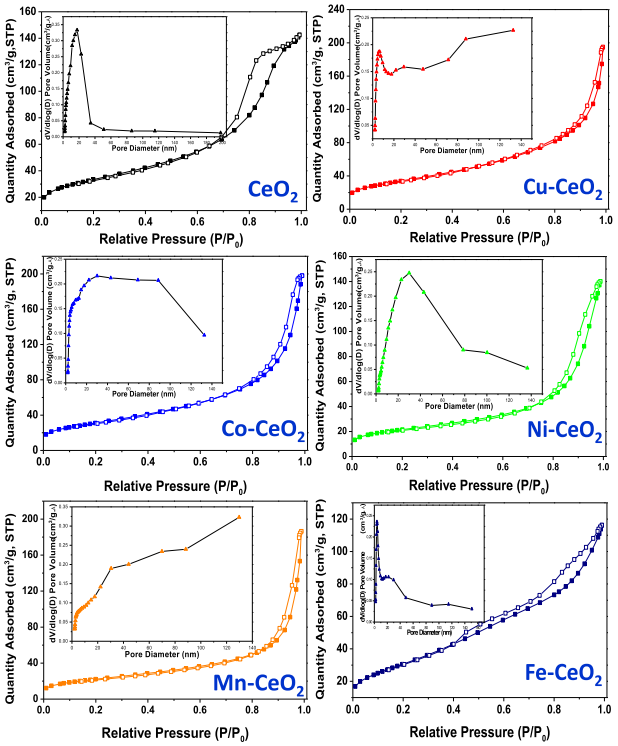

Figure 1. N_2 adsorption−desorption isotherm profiles of the heterostructured CeO_2-based nanocatalysts with associated pore size distribution profiles (as inset).

Table 1. Physical and Textural Properties of Heterostructured CeO_2-Based Nanocatalysts

entry	catalysts[a]	amount (wt %)[b]	SA_{BET} (m^2/g)	V_{Pore} (cm^3/g)	D_{Pore} (nm)
1	CeO_2		119.9	0.222	8.84
2	Cu−CeO_2	17.8	123.3	0.311	10.76
3	Co−CeO_2	18.3	112.7	0.315	11.68
4	Ni−CeO_2	19.1	76.8	0.216	14.69
5	Mn−CeO_2	18.5	80.7	0.288	16.23
6	Fe−CeO_2	18.7	112.7	0.195	6.35

[a]Base metals interfaced with CeO_2 are in the oxidized form. [b]Determined by inductively coupled plasma (ICP).

CeO_2 exhibited a type-IV isotherm with H_2 hysteresis loops associated with well-defined conical mesopores (Figure 1). The obtained BET surface area of CeO_2 was 119.9 m^2/g, having a total pore volume of 0.222 cm^3/g and a narrow pore size distribution profile centered at 8.84 nm (Table 1, entry 1). The heterostructured Cu−CeO_2, Co−CeO_2, Ni−CeO_2, and Mn−CeO_2 nanocatalysts showed type-IV isotherms with H_3 hysteresis loops. This indicated the formation of the mesoporous nature of these heterostructured CeO_2 interfaced composite nanocatalysts, characterized by partially filled slitlike pores in the framework structure.

The BET surface areas (SA_{BET}) of the heterostructured CeO_2 nanocatalysts were determined to be 76.8, 80.7, and 112.7 m^2/g, having corresponding total pore volumes of 0.216, 0.288, and 0.315 cm^3/g and pore diameters centered at 14.7, 16.2, and 11.7 nm for Ni−CeO_2, Mn−CeO_2, and Co−CeO_2, respectively. Cu−CeO_2 showed the highest BET surface area of 123.3 m^2/g, having a total pore volume of 0.311 cm^3/g and a pore diameter centered at 10.76 nm. In contrast, the Fe−CeO_2 was type-IV with an H_4 loop associated with the filled

https://dx.doi.org/10.1021/acsomega.9b04396
ACS Omega 2020, 5, 9775−9788

micropore structure. The BET surface area of Fe−CeO_2 was determined to be 112.7 m^2/g, whereas its total pore volume and pore diameter were 0.195 cm^3/g and 6.3 nm, respectively. Overall, the obtained N_2 physisorption data of the hetero-structured CeO_2 with respective base metal oxide nanocatalysts forming heterojunction interfaces were closely similar to the results attained for the pristine CeO_2 oxide. The respective amounts of the base metal contents in the interfaced heterostructured CeO_2 nanocatalysts are summarized in Table 1. The base metals as determined by the ICP were closely related to the nominal loading amount of 20 wt %.

Powder X-ray Diffractometry (XRD) Analysis. Figure 2 shows the XRD patterns and phase analyses of the pristine

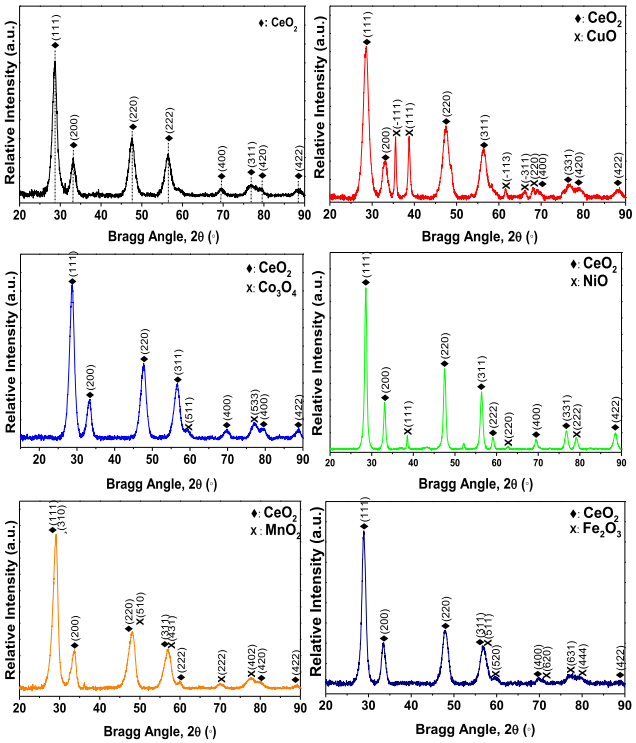

Figure 2. XRD patterns of the heterostructured CeO_2-based metal oxide nanocatalysts.

CeO_2 and heterostructured CeO_2-based nanocatalysts. The XRD patterns of CeO_2 confirm the formation of a typical cubic fluorite structure with strong intense diffraction peaks at 2θ = 28.5, 33.1, 47.5, 56.3, 59.1, 69.4, 76.7, 79.1, and 88.4°, which correspond to JCPDS PDF Card No: 34-0394, and arise from the (111), (200), (220), (311), (222), (400), (331), (420), and (422) crystal planes, respectively.[25,26] Similar strong diffraction peaks arising from CeO_2 were observed for the heterostructured CeO_2 metal oxide interfaced nanocatalysts, but they were noticeably shifted compared to those of the pristine CeO_2 (Figure S1). The Cu−CeO_2 showed additional diffraction peaks attributed to the monoclinic CuO phase (JCPDS PDF Card No: 05-0661).[27] The additional diffraction peaks observed for Co−CeO_2, Fe−CeO_2, and Ni−CeO_2 were attributed to the respective cubic structures of Co_3O_4 (JCPDS PDF Card No: 42-1467),[28] Fe_2O_3 (JCPDS PDF Card No: 39-1346),[29] and NiO (JCPDS PDF Card No: 47-1049),[30] respectively. Furthermore, the pattern of the Mn−CeO_2 catalyst exhibited extra peaks at 2θ = 71.2 and 77.2°, which correspond to the (222) and (402) crystal phases of the tetragonal α-MnO_2 phase (JCPDS PDF Card No: 44-0141).[31] The obtained XRD analysis results clearly demonstrate that the metal oxides had been successfully incorporated within the crystalline matrix of CeO_2. This was also shown by the associated shift in the CeO_2 (111) peak, as shown in Figure S1, compared to those of the individual metal oxides used to prepare the heterostructured CeO_2 interfaced composite nanocatalysts.

UV−Vis Spectroscopy Analysis. The optical properties of the pristine CeO_2 and heterostructure CeO_2-based nano-catalysts were examined by UV−vis spectroscopy. Figure 3a

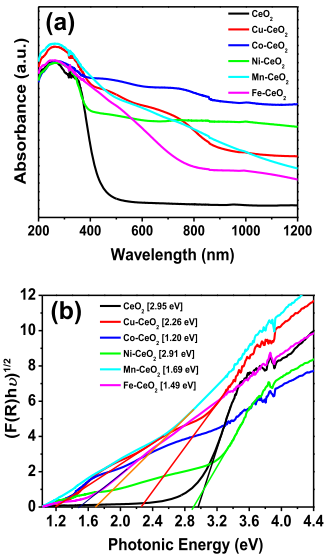

Figure 3. (a) UV−vis/NIR spectra and (b) Tauc plots of the heterostructure CeO_2-based metal oxide interfaced nanocatalysts.

shows the UV−vis absorption results of the heterostructured CeO_2-based nanocatalysts. Both the CeO_2 and heterostructured CeO_2-based nanocatalysts exhibited a red shift with a respective relative increase in the absorption range in the visible-light region. The associated optical band-gap energy (E_g) was calculated based on the absorbance spectrum of the nanocatalysts using the equation $E_g = 1240/\lambda_{Abs.Edge}$ and resolved using the Kubelka−Munk function, $[F(R_\infty)h\upsilon]^{1/2}$ (Figure 3b). The band-gap absorption onset of CeO_2 was determined to be 420 nm, which corresponds to a band energy of 2.95 eV. This shows that a red shift has occurred for the nanocatalyst CeO_2 compared to its bulk counterpart (E_g = 3.19 eV),[32] thus lowering its band-gap energy. This observation contrasts with other reported results in the literature, where a blue shift in the band gap arising from quantum confinement effects was observed.[32,33] However, the red shift is believed to originate from electron−phonon coupling, and the coefficient of this coupling increases with decrease in particle size.[34] It has been suggested that the formation of localized band-gap states is due to the presence of oxygen vacancies (V_o) and Ce^{3+} ions in the CeO_2 framework, which cause the observed red shift.[34] Other studies have reported that the blue shift is due to size effects, whereas the red shift is associated with the shape or morphology of the nanomaterial.[34] Thus, the origin of this phenomenon requires clarification, and more studies are required. The pristine CeO_2 exhibited a strong near-visible-light response in the violet region of the spectrum, which accounts for a small portion of the visible-light region. On the

https://dx.doi.org/10.1021/acsomega.9b04396
ACS Omega 2020, 5, 9775−9788

other hand, the heterostructured CeO_2 interfaced nanocatalysts containing Co, Cu, Ni, Fe, and Mn oxides exhibited an improved red shift in the band-gap energy compared to the pristine CeO_2. The band-gap energy of the heterostructured CeO_2-based metal oxide nanocatalysts resulted in a photocatalytic response to visible light (approximately ±420−800 nm), which is better than that of the pristine CeO_2 (420 nm) (Figure 3a). The absorption band edges of the respective heterostructured CeO_2-based metal oxide nanocatalysts were determined to be 426 nm (Ni−CeO_2), 549 nm (Cu−CeO_2), 734 nm (Mn−CeO_2), 832 nm (Fe−CeO_2), and 1033 nm (Co−CeO_2), and these absorption band edges correspond to band-gap energies of 2.91 eV (Ni−CeO_2), 2.26 eV (Cu−CeO_2), 1.69 eV (Mn−CeO_2), 1.49 eV (Fe−CeO_2), and 1.20 eV (Co−CeO_2). The high optical absorption efficiency displayed by the heterostructured CeO_2-based nanocatalysts compared to pristine CeO_2 indicates that more photoinduced electron−hole pairs are generated under visible-light irradiation, which could result in enhanced photocatalytic performance because of the efficiently separated electrons and holes and recombination suppression.

Photoluminescence (PL) Spectroscopy Analysis. Following the determination of the absorption range efficiency of the fabricated heterostructured CeO_2-based nanocatalysts, we further extended the investigation to probe the efficiency of electron−hole pair trapping, migration, and transfer in the semiconductor oxide particles using the PL analysis technique. The PL emissions originate from the radiative recombination of the photogenerated charge carriers; thus, there is a strong correlation between the PL intensity and photocatalytic activity. Figure 4 shows the PL spectra of the pristine CeO_2 and heterostructured CeO_2-based nanocatalysts obtained at an excitation wavelength of 325 nm. The deconvoluted emission peaks of the neat CeO_2 were found at 380, 407, 418, 432, 445, 469, 478, 507, and 655 nm with corresponding band-gap energies of 3.26, 3.05, 2.97, 2.87, 2.79, 2.64, 2.59, 2.45, and 1.89 eV (Figure S2). The neat CeO_2 showed strong violet/blue PL emission peaks (400−500 nm) associated with the radiative recombination of free electrons in shallow traps and sub-bands below the conduction band and free holes at the valence band edge. The significant blue-green PL emission peak (500−600 nm) can be attributed to the existence of surface defects with associated oxygen vacancies in the structure of the CeO_2 photocatalyst.[34,35] In contrast, the orange-red PL emission peaks (600−750 nm) can be ascribed to charge recombination on the localized band-gap states created by the existence of Ce^{3+} within the CeO_2 matrix.[34] The heterostructured CeO_2-based metal oxide interfaced nanocatalysts exhibited relatively similar PL emission peaks to those of neat CeO_2 but with different PL signal intensities (Figure 4). For instance, the Co−CeO_2 nanocatalyst exhibited the lowest PL signal, suggesting improved radiative recombination suppression compared to those of the CeO_2, Cu−CeO_2, Ni−CeO_2, Mn−CeO_2, and Fe−CeO_2 nanocatalysts. In contrast, Cu−CeO_2 had the highest PL emission intensities, indicating a decrease in the charge recombination suppression rate. In addition, the incorporation of Cu^+ ions into the CeO_2 matrix could lead to the formation of new recombination sites, thus increasing the PL intensity of the nanocatalyst.[36] Based on the PL data, the charge recombination suppression rate is influenced by the type of the base metal ion introduced into the CeO_2 structure framework. The suppression efficiencies in the pristine CeO_2 and heterostructure CeO_2-based nanocatalysts were tentatively determined to decrease in the order Co−CeO_2 > Mn−CeO_2 ≈ Ni−CeO_2 > Fe−CeO_2 > Cu−CeO_2 > CeO_2.

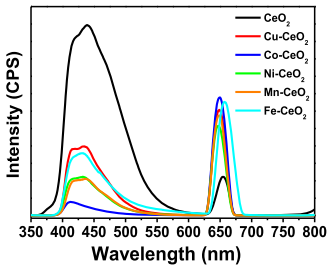

Figure 4. Photoluminescence spectra of various heterostructured CeO_2-based photocatalysts.

Scanning Electron Microscopy (SEM) and Transmission Electron Microscopy (TEM) Analyses. Figure 5 presents SEM images of the pristine CeO_2 and heterostructured CeO_2-based nanocatalysts. The SEM micrograph of CeO_2 reveals the formation of spherical particles with particle diameters ranging from 20 to 50 nm. The introduction of the different base metal ions into the CeO_2 structure resulted in significantly different morphologies. The Co−CeO_2, Ni−CeO_2, Mn−CeO_2, and Fe−CeO_2 nanocatalysts showed a slight increase in their respective particle size dimensions while maintaining the observed pristine CeO_2 spherical shape morphology with slightly roughened edges. Overall, the mean diameters of the Co−CeO_2, Ni−CeO_2, Mn−CeO_2, and Fe−CeO_2 particles were determined to be 60−76 nm. The Cu−CeO_2 exhibited an increase in the particle size with an approximate diameter of 127 nm.

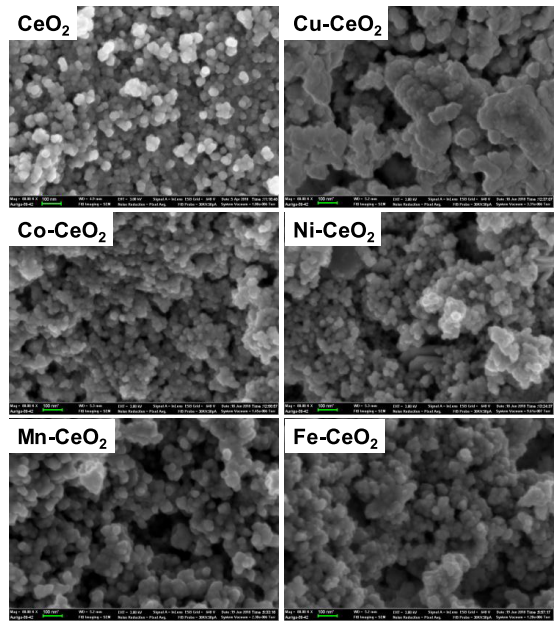

Figure 5. SEM images of heterostructured CeO_2 interfaced nanocatalysts.

The nanostructure morphology, crystallinity, and dimensions of the neat CeO_2 and heterostructured CeO_2 interfaced nanocatalysts were examined by TEM, high-resolution (HR)-TEM, and selected area electron diffraction (SAED) analyses. The TEM images (Figure 6a) reveal a mixed morphology of

https://dx.doi.org/10.1021/acsomega.9b04396
ACS Omega 2020, 5, 9775−9788

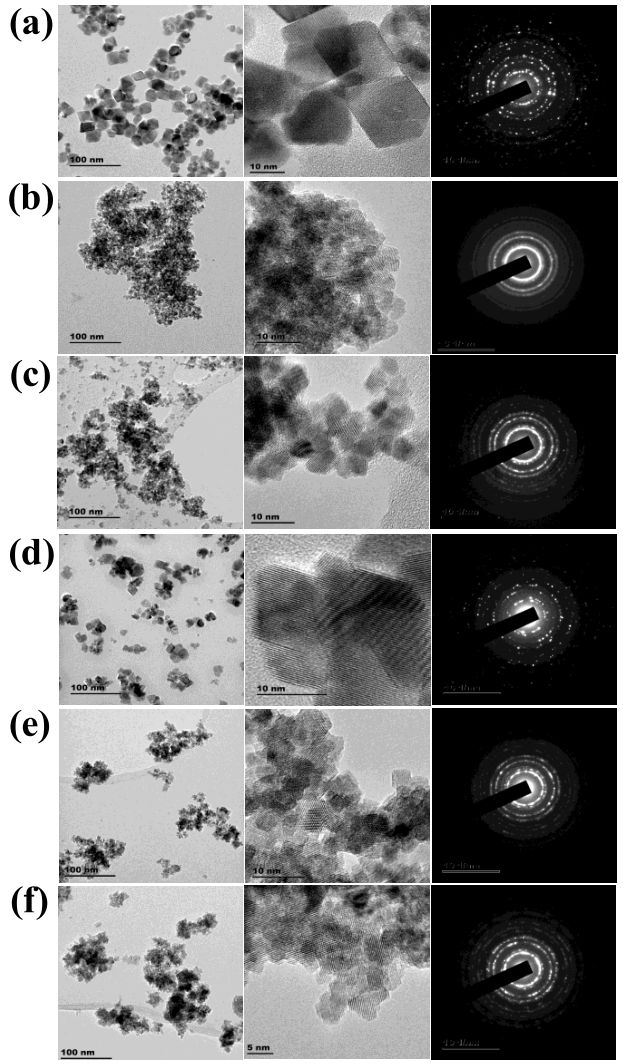

Figure 6. TEM/HRTEM images and SAED patterns of (a) CeO_2, (b) Cu−CeO_2, (c) Co−CeO_2, (d) Ni−CeO_2, (e) Mn−CeO_2, and (f) Fe−CeO_2 heterostructured nanocatalysts.

spherical and rhombohedral particles, where the dominant morphology was rhombohedral. The average particle size of the rhombohedral CeO_2 nanocatalyst was found to be 25.4 nm. Further investigation using HRTEM revealed the interplanar spaces of 0.3191 and 0.3105 nm, which correspond to the (111) crystal facets of the CeO_2 nanocatalyst. Figure 6b shows the TEM, HRTEM, and SAED images of the Cu−CeO_2 photocatalyst. The data indicate a highly agglomerated sample made up of small irregular particles having a mean diameter of 5.6 nm (Figure 6b). Moreover, the HRTEM images indicate interplanar distances of 0.3200 and 0.3110 nm, which correspond to the CeO_2 (111) planes. However, no interplanar spacings attributed to CuO were observed, which indicates the presence of weak interactions between the CeO_2 and CuO particles. Moreover, the SAED pattern indicates that the Cu−CeO_2 nanocatalyst was polycrystalline. The Co−CeO_2 nanocatalyst morphology and crystallinity were examined by TEM, HRTEM, and SAED analyses, as shown in Figure 6c. The TEM images show spherical particles with an average diameter of 6.7 nm that have agglomerated to form larger clusters. Figure 6d shows the TEM and SAED patterns of the Ni−CeO_2 nanocatalyst. The TEM image shows small irregular particles with rhombohedral particles making up the majority of the sample. The average particle diameter was found to be 29.0 nm, and the SAED analysis revealed the polycrystalline structure of the Ni−CeO_2 nanocatalyst. The Mn−CeO_2 photocatalyst morphology and crystallinity were also examined by TEM, HRTEM, and SAED analyses, as shown in Figure 6e. The TEM images show small irregular particles having an average size of 6.0 nm. The particles are highly agglomerated to form islands of clusters of average size of 88.3 nm. Furthermore, the SAED pattern indicates that the Mn−CeO_2 nanocatalyst has a polycrystalline structure. Figure 6f shows the TEM and SAED images of the Fe−CeO_2 nanocatalyst. The TEM image shows small irregular particles having a mean diameter of 5.7 nm that are highly packed together. Moreover, the SAED analysis illustrates a polycrystalline structure of the Fe−CeO_2 nanocatalyst.

X-ray Photoelectron Spectroscopy (XPS) Analysis. The oxidation state of the elements and surface composition of CeO_2 and the heterostructure CeO_2 interfaced catalysts were investigated using the XPS technique. Figure 7 shows the high-resolution XPS spectra of the Ce 3d core level and the corresponding peak fitting results of the catalyst samples. All of the heterostructure catalysts exhibited the eight binding energy (BE) peaks associated with the Ce 3d electrons of Ce corresponding to four pairs of spin−orbit doublets.[37] As shown in Figure 7a, CeO_2 exhibited five BE peaks at 882.1 (ν), 888.4 (ν''), 898.2 (ν'''), 907.3 (υ''), and 916.4 eV (υ'''), which are attributed to the Ce^{4+} 3d final states, while the three BE peaks at 884.5 (ν'), 900.5 (υ°), and 902.8 eV (υ') are attributed to the Ce^{3+} 3d final states.[38] The results show the CeO_2 to consist mostly of the Ce^{4+} ions. The heterostructure CeO_2 catalysts exhibited similar BE peaks associated with the coexistence of Ce^{4+} and Ce^{3+} ions (Figure 7b−f).

It is known that the Ce^{3+} concentration can be correlated to the oxygen vacancies on the surface of the catalyst, which are created when Ce(IV) ions are transformed to Ce(III) ions, thus leading to the formation of oxygen vacancies. As a result, the amount of surface Ce^{3+} ions can be estimated using the following equation

$$C_{Ce^{3+}} = \frac{Ce^{3+}}{Ce} = \frac{Ce^{3+}}{Ce^{3+} + Ce^{4+}} = \frac{\nu^\circ + \nu' + \upsilon^\circ + \upsilon'}{(\nu^\circ + \nu' + \upsilon^\circ + \upsilon') + (\nu + \nu'' + \nu''' + \upsilon + \upsilon'' + \upsilon''')} \times 100 \quad (1)$$

where $Ce^{3+} = \nu^\circ + \nu' + \upsilon^\circ + \upsilon'$ and $Ce^{4+} = \nu + \nu'' + \nu''' + \upsilon + \upsilon'' + \upsilon'''$. The Ce^{3+} ion concentrations were determined to be 34.5, 48.4, 10.5, 43.7, 40.2, and 45.1% for the neat CeO_2, Cu−CeO_2, Co−CeO_2, Ni−CeO_2, Mn−CeO_2, and Fe−CeO_2 nanocatalysts, respectively. The high-resolution XPS spectra of the O 1s core level confirmed the presence of surface oxygen vacancies (V_o) in the CeO_2 matrix (Figure 7a). Further, CeO_2 exhibited three O 1s BE peaks at 529.2, 530.3, and 531.2 eV associated with the lattice oxygen (O_L), oxygen vacancies (O_V), and absorbed oxygen (O_A), respectively (Figure 7a). The XPS data indicated that the introduction of the various metals onto CeO_2 induced significantly varying effects on the V_o concentration on the surface of CeO_2. The surface V_o concentration of the nanocatalyst samples can be evaluated using the O_V/O_L ratio. As a result, the O_V/O_L ratio was determined to be 0.78, 1.65, 0.98, 1.45, 0.52, and 0.97 for the neat CeO_2, Cu−CeO_2, Co−CeO_2, Ni−CeO_2, Mn−CeO_2, and Fe−CeO_2 nanocatalysts, respectively (Table 2). From the XPS

https://dx.doi.org/10.1021/acsomega.9b04396
ACS Omega 2020, 5, 9775−9788

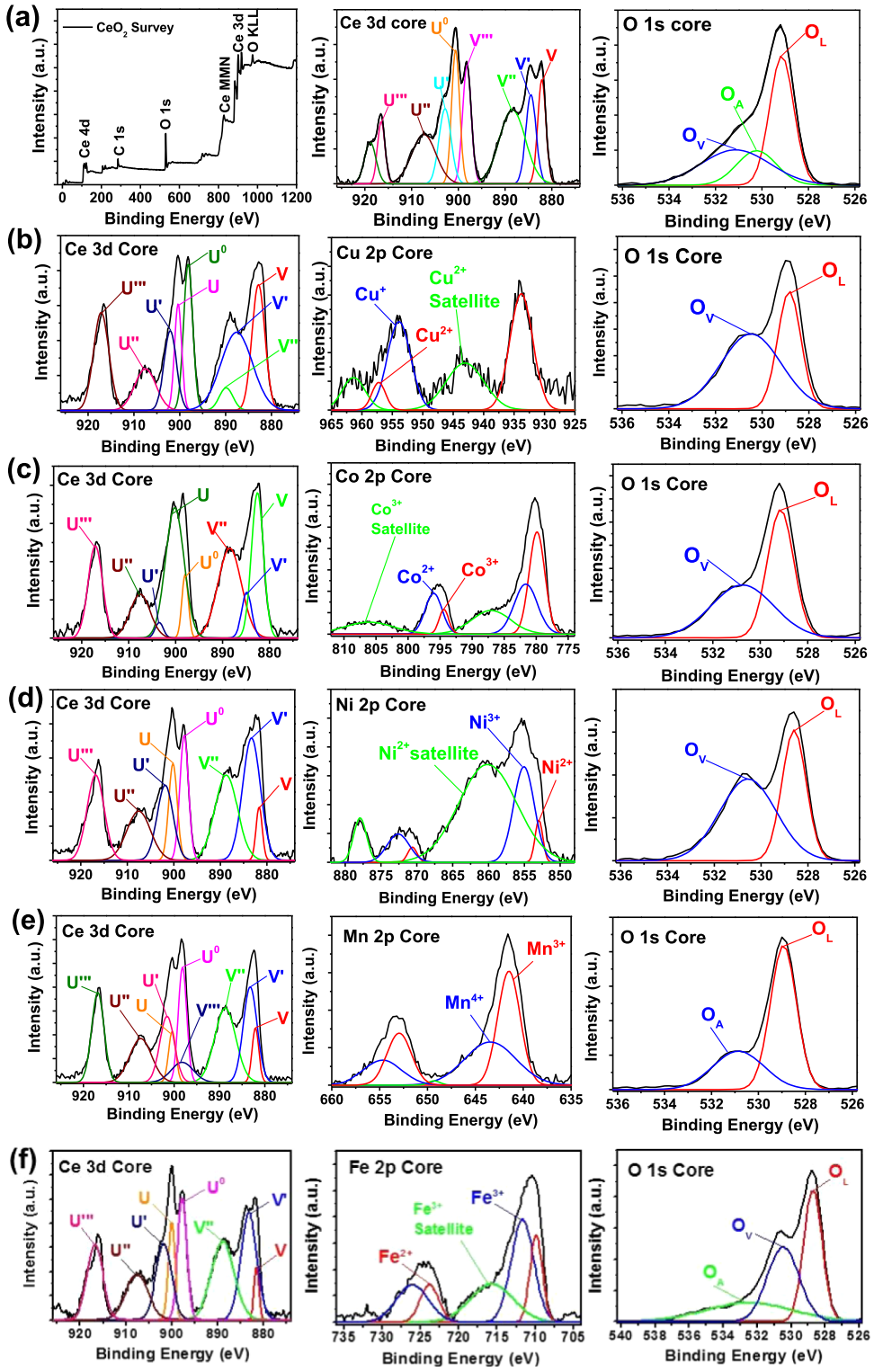

Figure 7. XPS spectra of (a) CeO_2, (b) Cu−CeO_2, (c) Co−CeO_2, (d) Ni−CeO_2, (e) Mn−CeO_2, and (f) Fe−CeO_2 heterostructured nanocatalysts.

data, the Cu−CeO_2 catalyst exhibited the highest surface V_o concentration compared to the other heterostructured CeO_2 catalysts. The 2p core of all the base metal (Cu, Co, Ni, Mn, and Fe) oxides interfaced with CeO_2 appeared as spin−orbit doublets. The high-resolution XPS spectra of Cu 2p gave peaks at 933.8 eV ($2p_{3/2}$) and 954.3 eV ($2p_{1/2}$) assigned to the spin−orbit doublets. Besides the Cu 2p peaks, two additional peaks at 943.0 and 961.2 eV were also observed. The obtained Cu oxide in the composite was predominantly in the higher 2+ oxidation state (Cu^{2+} = 73.4%). Furthermore, the ratio of Cu to Ce ions was determined to be 0.18. The Co−CeO_2 catalyst exhibited peaks at 780.6 eV ($2p_{3/2}$) and 795.3 eV ($2p_{1/2}$) and two additional satellite peaks at 788.1 and 804.2 eV. The deconvoluted peaks of Co $2p_{3/2}$ at 781.2 and 783.5 eV are

https://dx.doi.org/10.1021/acsomega.9b04396
ACS Omega 2020, 5, 9775−9788

Table 2. Summarized XPS Data for Neat CeO_2 and Heterostructured CeO_2-Based Nanocatalysts

	catalyst[a]	Ce 3d core		O 1s core		M core	
entry		Ce^{3+} (%)	Ce^{3+}/Ce^{4+}	O_V (%)	O_V/O_L	M (%)	M/Ce
1	CeO_2	34.5	0.53	35.2	0.78		
2	$Cu-CeO_2$	48.4	0.94	62.3	1.65	15.0	0.18
3	$Co-CeO_2$	10.5	0.12	49.5	0.98	26.0	0.35
4	$Ni-CeO_2$	43.7	0.77	59.3	1.45	25.2	0.34
5	$Mn-CeO_2$	40.2	0.67	34.2	0.52	11.5	0.13
6	$Fe-CeO_2$	45.1	0.82	36.8	0.97	17.5	0.21

[a]The base metals interfaced with CeO_2 are in the oxide form. Symbols: O_V, oxygen vacancies; O_L, lattice oxygen.

ascribed to the presence of the Co^{3+} and Co^{2+} ions. The Co oxide in the heterostructured $Co-CeO_2$ nanocatalyst was found to be mainly in the higher Co^{3+} oxidation state (Co^{3+} = 67.9%). The $Ni-CeO_2$ nanocatalyst exhibited peaks at 855.2 eV (Ni $2p_{3/2}$) and 873.1 eV (Ni $2p_{1/2}$) and shake-up peaks at 859.6 and 877.4 eV, an indication that the obtained Ni oxide was in the lower 2+ oxidation state (Ni^{2+} = 65.9%). However, the $Mn-CeO_2$ catalyst showed peaks at 641.8 eV ($2p_{3/2}$) and 652.9 eV ($2p_{1/2}$). The deconvoluted peaks of Mn $2p_{3/2}$ situated at 640.7 and 642.8 eV correspond to the Mn^{3+} and Mn^{4+} oxidation states; the estimation of the peak areas revealed that the sample contained slightly more of the Mn^{3+} ions present in the crystal structure (Mn^{3+} = 55.9%). Lastly, the $Fe-CeO_2$ catalyst exhibited peaks at 710.4 eV ($2p_{3/2}$) and 724.8 eV ($2p_{1/2}$) and an additional peak at 716.2 eV. The deconvoluted peaks of Fe $2p_{3/2}$ located at 709.8 and 711.7 eV represent the Fe^{2+} and Fe^{3+} oxidation states. The estimated peak areas of the respective deconvoluted peaks confirmed the presence of the higher Fe^{3+} as the major oxidation state (Fe^{3+} = 69.2%).

Electron Paramagnetic Resonance (EPR) Analysis. EPR has been widely employed to determine the nature and the environment of paramagnetic species having one or more unpaired electrons, either in the bulk or on the surface of various solid catalysts. Further, it has been utilized to confirm the presence of the solid material defect structures. Figure 8

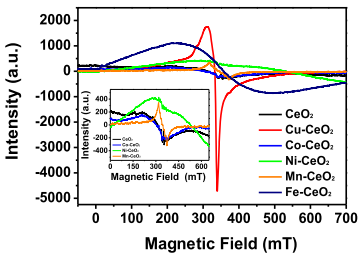

Figure 8. EPR spectra of the heterostructure CeO_2 interfaced nanocatalysts.

shows the X-band EPR spectra of the CeO_2 and heterostructure CeO_2 interfaced catalysts acquired at ambient temperature. The spectra of CeO_2 exhibited EPR signals with g values in the range of 2.022−2.034, which are attributed to the presence of adsorbed superoxo species, O_2^- with one unpaired electron. Oxygen species can be adsorbed onto Ce^{4+} ions or can fill oxygen vacancies, thus forming surroundings with different symmetries and resulting in different EPR signals. O_2^- species on the surface of CeO_2 originate from the adsorbed O_2 on either isolated or associated oxygen vacancies. As a result, the observed EPR signal g = 2.03 represents the $Ce^{4+}-O_2^-$ complexes, where O_2^- is adsorbed on isolated vacancies. Further, additional EPR signals g = 1.96 and 1.94 are also observed in the CeO_2 sample. These EPR signals could be assigned to Ce^{3+} ions associated with the anion vacancies but could also originate from the F^+ centers. The EPR signals at g = 1.91 and g = 1.88 are ascribed to the defect paramagnetic state such as the vacancy trapped electron, since the g value was less than that of a free electron.[39] The heterostructure CeO_2 interfaced catalysts showed different EPR signals depending on the type of base metal oxide used. The $Cu-CeO_2$ catalyst exhibited the sharpest EPR signal among the heterostructure CeO_2 catalyst samples. The EPR signal (g = 1.94) can be attributed to the Ce^{3+} ions in the $Cu-CeO_2$ nanocatalyst. Furthermore, the EPR signal at g = 2.14 can be assigned to Cu^{2+} ions present in the amorphous clusters or aggregates.[40] The $Fe-CeO_2$ catalyst exhibited a broadband EPR signal attributed to the dipolar interaction between the Fe^{3+} ions in the crystal matrix. The EPR spectrum observed for $Mn-CeO_2$ constituted a broad signal with a peak-to-peak distance of ∼53 mT superimposed on a weak-intensity signal with a hyperfine structure of six lines centered at g = 2.004, which is closer to the free electron value and can be assigned to unpaired electrons trapped in oxygen vacancies, namely, F^+ centers.[41−43]

Photocatalytic Oxidation of Pinene. The photocatalytic activities and selectivities of the heterostructured CeO_2-based catalysts were evaluated for the photooxidation reaction of pinene to various aroma oxygenates. The obtained catalytic results are presented in both Figure 9 and Table 2, respectively.

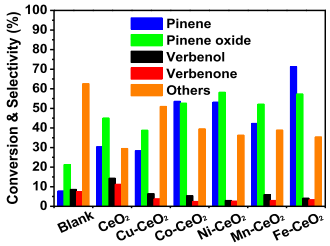

Figure 9. Screening of the photocatalytic activity of the heterostructure CeO_2 catalysts in pinene oxidation. Reaction conditions: pinene (10 mmol; 1.36 g), catalyst (0.10 g), acetonitrile (125 mL), T = 25 °C, and t = 5 h.

There are two distinct reaction pathways that can occur during the oxidation reaction of pinene: allylic oxidation and the epoxidation of the inert C−H bond, as illustrated in Scheme 1.[1,4,37] The reaction pathways of the photoinduced noncatalytic oxidation of pinene without a catalyst were also investigated. It was found that epoxidation is the predominant reaction pathway because pinene oxide was obtained as the major product of the pinene oxidation reaction. For the nonphotocatalytic oxidation reaction, a low pinene conversion

https://dx.doi.org/10.1021/acsomega.9b04396
ACS Omega 2020, 5, 9775−9788

Scheme 1. Plausible Reaction Pathways Involved in the Oxidation of Pinene

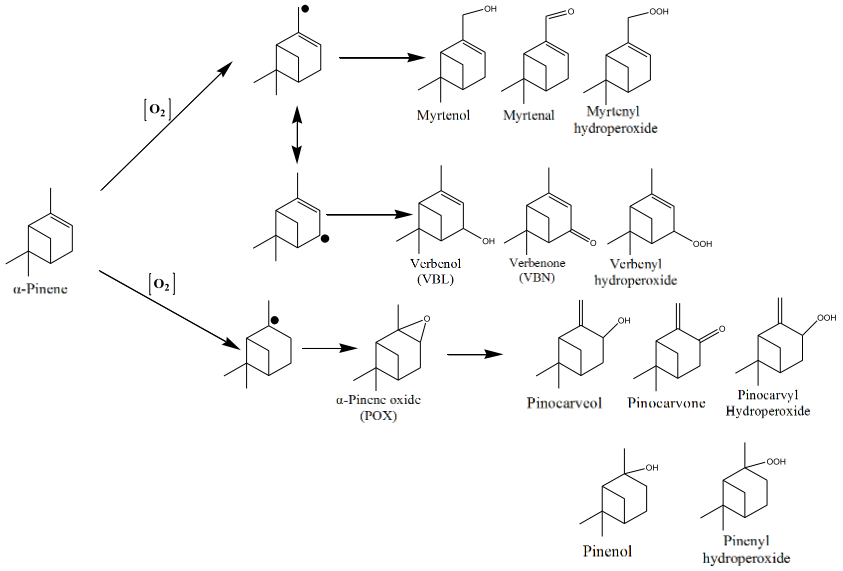

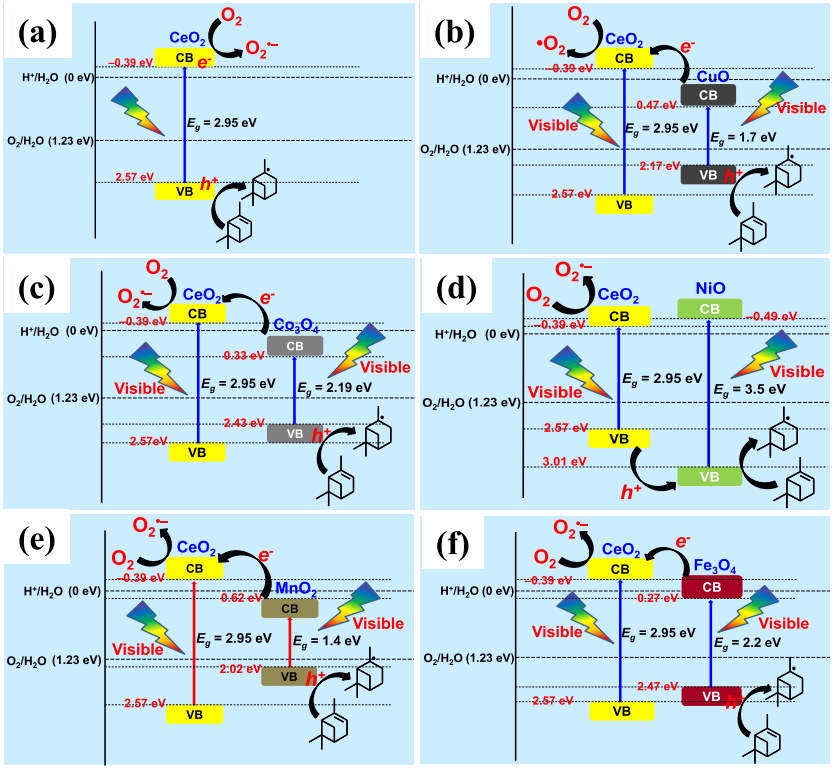

Figure 10. Plausible electron transfer mechanism of heterostructured CeO_2-based metal oxide interfaced nanocatalysts under visible-light irradiation: (a) CeO_2, (b) Cu−CeO_2, (c) Co−CeO_2, (d) Ni−CeO_2, (e) Mn−CeO_2, and (f) Fe−CeO_2.

of 7.8% yielding 21.3% pinene oxide was obtained. Furthermore, although epoxidation was the predominant reaction pathway, the product distribution indicated the simultaneous occurrence of both mechanisms (i.e., allylic oxidation and epoxidation). This was shown by the highly nonselective reaction leading to a large number of side oxidation products for the nonphotocatalyzed reaction other than the usual major products of verbenone and verbenol. The nonselective nature of the uncatalyzed reaction could be attributed to the resonance stability of the pinene allyl radical nature, thus leading to a wide range of reaction pathways, yielding verbenyl, pinenyl, pinocarvyl, and myrtenyl products (Scheme 1).[37]

When the CeO_2 nanocatalyst was used for the photooxidation reaction, the pinene conversion (30.4%) improved significantly to almost four times that of the nonphotocatalyzed reaction. Similarly, the selectivity toward the formation of pinene oxide increased to 45.0% (Figure 9 and Table 2, entry 1). Notably, the pure CeO_2 showed greater improvement in the selectivity toward verbenone and verbenol compared to the noncatalyzed reaction and other heterostructured CeO_2 nanocatalysts. Upon visible-light irradiation, the electrons

https://dx.doi.org/10.1021/acsomega.9b04396
ACS Omega 2020, 5, 9775−9788

Table 3. Product Distribution for the Photooxidation Reaction of Pinene over Heterostructured CeO_2-Based Catalysts

	catalyst[a]		selectivity (%)			
entry		conversion (%) pinene	pinene oxide	verbenol	verbenone	others
1	blank	7.8	21.3	8.6	7.5	62.6
2	CeO_2	30.4	45.0	14.3	11.2	29.5
3	Cu−CeO_2	28.4	38.8	6.4	3.8	51.0
4	Co−CeO_2	53.6	52.6	5.4	2.5	39.5
5	Ni−CeO_2	53.1	58.2	3.0	2.6	36.3
6	Mn−CeO_2	42.3	52.1	6.0	3.0	38.9
7	Fe−CeO_2	71.3	57.3	4.1	3.3	35.4

[a]The base metals interfaced with CeO_2 are in the oxide form. Other reaction conditions: pinene (10 mmol; 1.36 g), catalyst (0.10 g), acetonitrile (125 mL), T = 25 °C, and t = 5 h.

Scheme 2. Plausible Reaction Pathways Involved in the Catalytic Oxidation of Pinene to Pinene Oxide and its Subsequent Isomerization Products

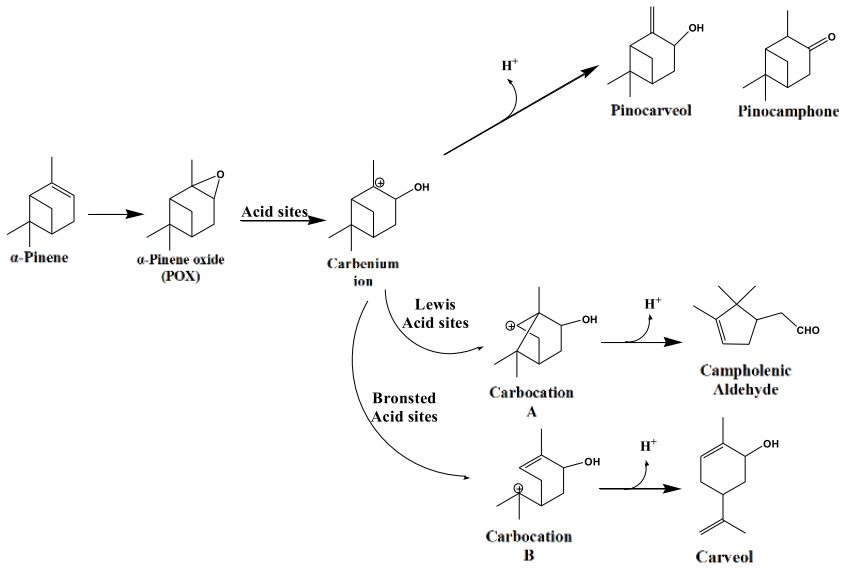

(e^-) from the valence band (VB) are transported to the conduction band (CB) of CeO_2, where they are scavenged by the introduced O_2 molecules, thus creating positive holes (h^+) in the VB of CeO_2. At the surface, the reaction of the e^- with O_2 generates the superoxide anion ($^{\bullet}O_2^-$) radicals, which are capable of initiating the free-radical-driven oxidation reaction by abstracting the H-atom from the chiral carbon of pinene to produce the allyl radicals of α-pinene. The pinene allyl radicals are resonance stabilized, leading to the formation of verbenyl, pinenyl, pinocarvyl, and myrtenyl products. Furthermore, $^{\bullet}O_2^-$ reacts with H^+ to produce the peroxyl radical (HOO$^{\bullet}$). The formed HOO$^{\bullet}$ radical can react with the pinene allyl radicals to form pinene oxide and hydroperoxide-derived products of the verbenyl, pinenyl, pinocarvyl, and myrtenyl intermediates. The remaining h^+ in the VB can react with the α-pinene to form more allyl radicals or be quenched by the solvent. It is likely that the $^{\bullet}$OH radicals (+2.80 eV) are not produced during this reaction because of the nonaqueous reaction medium and the VB position (+2.57 eV) of CeO_2, as illustrated in Figure 10. Interestingly, there was a decrease in the formation of side products when CeO_2 was used, and the selectivity dropped from 62.6 to 29.5% (Table 3, entries 1 and 2). The photocatalytic results showed that pinene oxide was the major product of the CeO_2-catalyzed reaction.

Moreover, there is strong evidence that the isomerization products of pinene oxide such as pinocarveol, pinocamphone, carveol, and campholenic aldehyde (not analyzed) could be present in the oxidation product mixture, as shown in Scheme 2. CeO_2 possesses both acidic and basic active sites, and these could play an important role in determining the product selectivity in pinene oxidation reactions. Such active acidic sites in CeO_2 could lead to the activation of the epoxy ring (C−O−C) of pinene oxide to form a carbenium ion, which could yield dehydrogenation products such as pinocarveol and pinocamphone.[1] In addition, the carbenium ion can be rearranged to form a carbocation depending on the nature of the active acid sites (Brønsted or Lewis acidic). Campholenic aldehyde can be obtained by the cleavage of the C_2−C_3 bond of the cation, whereas carveol can be obtained from the proton shift of the C_9 methyl group of the cation.[1,33] However, the photoactivity and selectivity for pinene oxidation over CeO_2 were lower than those of the heterostructured CeO_2 nanocatalysts. This could be ascribed to the limitations of CeO_2 as a photocatalyst with respect to poor charge migration, which leads to charge recombination and, thus, insufficient photocatalytic performance. In addition, the broadband PL emission (380−550 nm) indicates the occurrence of both the photocatalytic irradiative recombination of shallow trapped e^- in the sub-bands below the CB and h^+ in the VBM, as well as charge recombination because of the existing surface defects with associated V_o in the CeO_2 matrix.

https://dx.doi.org/10.1021/acsomega.9b04396
ACS Omega 2020, 5, 9775−9788

The tentative interparticle electron transfer mechanism for the heterostructured CeO_2-based nanocatalysts is presented in Figure 10. The band edge position of the CB and VB of a semiconductor can be evaluated using eqs 2−4.

$$E_{CB} = \chi - E^c - 0.5E_g \quad (2)$$

$$E_{VB} = E_{CB} + E_g \quad (3)$$

$$\chi = [\chi^a \chi^b \chi^c]^{1/(a+b+c)} \quad (4)$$

Here, E_{CB} and E_{VB} are the CB and VB potentials, respectively; E^c is the energy of free electrons vs the standard hydrogen electrode (4.5 eV); E_g is the band-gap energy of the semiconductor; χ is the absolute electronegativity of the semiconductor; and a, b, and c are the numbers of atoms in the compound. The absolute electronegativity of neat CeO_2 was calculated to be 5.59 eV, which is consistent with the literature value (5.56 eV).[17] Furthermore, the calculated CB and VB positions of CeO_2 were found to be −0.39 and 2.57 eV, respectively. The χ, E_{CB}, and E_{VB} values of the base metal oxide photocatalysts were estimated to be 5.82, 0.47, and 2.17 eV for CuO; 5.92, 0.33, and 2.52 eV for Co_3O_4; 5.76, 0.49, and 3.01 eV for NiO; 5.82, 0.62, and 2.02 eV for MnO_2; and 5.87, 0.27, and 2.47 eV for Fe_2O_3, respectively.

Figure 10 shows the band edges and types of the heterostructured CeO_2 interfaced nanocatalysts. Based on the data, all of the heterostructured CeO_2 composites interfaced with metal oxides (i.e., CuO, Co_3O_4, NiO, MnO_2, and Fe_2O_3) have type-I heterojunction interfaces, where the conduction band minimum (CBM) of the base metal oxide is lower than the CBM of CeO_2 and the valence band minimum (VBM) of the base metal oxide is higher than that of CeO_2.[44] However, the Ni−CeO_2 nanocatalyst displayed the opposite trend, i.e., the CBM of NiO is higher than that of CeO_2 and the VBM is lower. It is worth noting that the enhancement in the light absorption of the Ni−CeO_2 nanocatalyst could be attributed to the $Ni^{2+} \rightarrow Ce^{4+}$ charge transfer transition, which occurs at low photonic energy compared to the $O^{2-} \rightarrow Ce^{4+}$ charge transfer interaction. The sub-band called the $Ni^{2+} \rightarrow Ce^{4+}$ charge transfer band was caused by the Ni^{2+} 3d band situated between the CB formed due to Ce 3d orbitals and VB formed due to the O 2p orbitals of CeO_2.[45] During visible-light photoirradiation, the base metal oxides (Cu, Co, Mn, and Fe) act as the photosensitizer since they possess smaller band-gap energies compared to CeO_2. Typically, the photoexcited e^- in the base metal oxide can be transferred to the CB of CeO_2, where they can react with the O_2 to produce the $^{\bullet}O_2^-$. For example, in Cu−CeO_2, CuO has a lower CBM and a higher VBM than those of CeO_2 (Figure 10). As a result, during photoirradiation, the photoinduced e^- in the VB are transported to the CB of CuO where they then migrate to the CB of CeO_2. At the CB of CeO_2, the photoinduced e^- can react with O_2 to form $^{\bullet}O_2^-$, which attacks the pinene molecules to produce pinene allyl and $^{\bullet}$OOH radicals via H-atom abstraction. The $^{\bullet}$OOH radicals react with H^+ to form H_2O_2, which subsequently forms $^{\bullet}$OH. Simultaneously, the photogenerated h^+ left in the VB of CuO can react with pinene to form pinene allyl radicals or are quenched by the solvent. Clearly, a high level of charge recombination might have occurred during visible-light irradiation over Cu−CeO_2, as evidenced by its lower photoactivity and selectivity for the oxidation of pinene compared to CeO_2 or other heterostructured CeO_2 interfaced nanocatalysts (Figure 9 and Table 3, entry 3). Over the CuO−CeO_2 heterojunction, the conversion of pinene was found to be 28.4%, having selectivities of 38.8, 6.4, and 3.8% for pinene oxide, verbenol, and verbenone, respectively. The side-product formation accounted for the total selectivity of 51%. These include probable formation of side products such as isomerized intermediates (i.e., pinocarveol, pinocamphone, carveol, and campholenic aldehyde) and allylic intermediates (pinenyl, pinocarvyl, and myrtenyl). This is a strong indication that both pinene oxidation reaction pathways (allylic oxidation and epoxidation) may proceed simultaneously during pinene oxidation over Cu−CeO_2. The addition of Cu^+/Cu^{2+} ions into the CeO_2 matrix could lead to the introduction of new active acidic sites suitable for isomerization reactions. In addition, the CuO could act as a photosensitizer because it has a small band gap of 1.7 eV, which corresponds to a wavelength of ca. 730 nm and, thus, a strong visible-light response. Moreover, the lowered photoactivity observed for the Cu−CeO_2 photocatalyst could be attributed to the susceptibility of CuO to photocorrosion under light irradiation.[46]

A similar electron transfer mechanism to that of Cu−CeO_2 was observed for Co−CeO_2 (Figure 10). Unlike Cu−CeO_2, both the photocatalytic activity and selectivity improved significantly compared to those of pure CeO_2. The pinene conversion was found to be 53.6%, having selectivities of 52.6, 5.4, and 2.5% for pinene oxide, verbenol, and verbenone, respectively, for Co−CeO_2 (Figure 9 and Table 3, entry 4). However, the pinene conversion decreased slightly to 42.3% over Mn−CeO_2, having selectivities of 52.1, 6.0, and 3.0% for pinene oxide, verbenol, and verbenone, respectively (Figure 9 and Table 3, entry 6). Fe−CeO_2 exhibited the highest photocatalytic activity among all of the evaluated heterostructured CeO_2 interfaced nanocatalysts, having a pinene conversion of 71.3%. At 71.3% pinene conversion, the product selectivity distribution values were determined to be 57.3, 4.1, and 3.3% for pinene oxide, verbenol, and verbenone, respectively (Figure 9 and Table 3, entry 7). However, the highest pinene oxide selectivity of 58.2% was obtained with Ni−CeO_2 but at a lower pinene conversion of 53.1% compared to 71.3% of the Fe−CeO_2 nanocatalyst (Figure 9 and Table 3, entry 5). This could be attributed to a different electron transfer mechanism for Ni−CeO_2 even though NiO possesses a very large band-gap energy (~3.5 eV) and remains largely unexcited during visible-light irradiation. NiO is a well-known thermocatalyst and could be activated by the localized heating, which occurs during charge recombination. Also, p-type NiO can receive the photogenerated holes from VB of CeO_2 to be employed in the direct reaction with pinene molecules or quenching by the solvent. Simultaneously, the photoinduced e^- in the CB of CeO_2 react with the O_2 to form $^{\bullet}O_2^-$. $^{\bullet}O_2^-$ can then be protonated to form HOO$^{\bullet}$. Thus, the oxidation reaction is initiated on the surface of CeO_2. Further, the enhanced activity of NiO−CeO_2 could be ascribed to the improved electron/hole separation efficiency following the effect of the Schottky and p−n (SPN) heterojunction interface of the p-type NiO and n-type CeO_2 semiconductors. Such a constructed p−n interface has been shown to improve significantly on the photocatalytic activity with extended visible-range absorption for NiO-based heterojunction semiconductor photocatalysts.[47−49]

Overall, the ranking of the heterostructured CeO_2 photocatalysts based on pinene oxide selectivity is Ni−CeO_2 > Fe−CeO_2 > Co−CeO_2 > Mn−CeO_2 > Cu−CeO_2, whereas that for

https://dx.doi.org/10.1021/acsomega.9b04396
ACS Omega 2020, 5, 9775−9788

pinene conversion is Fe−CeO_2 > Co−CeO_2 > Ni−CeO_2 > Mn−CeO_2 > Cu−CeO_2 (Table 2). Based on the results obtained in this study, it is clear that efficient charge recombination suppression can be obtained when n-type CeO_2 is coupled with metal oxides such as Fe_2O_3 and NiO in the designed heterostructure photocatalysts, thus leading to improved photocatalytic activity. Moreover, traditional thermocatalysts such Fe_2O_3, NiO, and MnO_2 can assist in driving the product selectivity toward pinene oxide by introducing additional selective active sites. Most importantly, the addition of base metal oxides to CeO_2 as cocatalysts was seen to promote efficient charge electron/hole separation, thus enhancing the photocatalytic activity compared to the neat CeO_2. Furthermore, based on the XPS and EPR results, it is clear that the interface of CeO_2 with the base metal oxide cocatalysts presented significantly varying concentration amounts of the surface defect oxygen vacancies and electronic interactions with respective redox oxidation states. Such structure modification effects due to the interactions of CeO_2 with the respective base metal oxides contributed differently to the photocatalytic activity performances.

Catalytic Activity under Pinene Hydroperoxidation Conditions. To understand the structure−activity relationship of the heterostructured CeO_2 interfaced catalysts with respect to the oxyfunctionalization of the inert pinene C−H bond, we investigated their catalytic activity in the presence of added hydrogen peroxide (H_2O_2) in the conventional catalytic hydroxylation process. Figure 11 summarizes the obtained

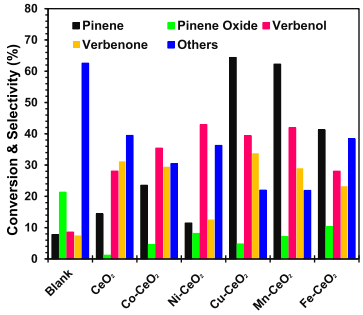

Figure 11. Screening the photoactivity of the heterostructured CeO_2 catalysts in the pinene hydroperoxidation reaction. Reaction conditions: pinene (10 mmol; 1.36 g), catalyst (0.10 g), 30% H_2O_2 (30 mmol), acetonitrile (12.5 mL), T = 65 °C, and t = 5 h.

catalytic performance results. The pinene oxidation reaction performed using CeO_2 showed inefficient catalytic activity, achieving 13.5% conversion. Among the heterostructure CeO_2 nanocatalysts, Ni−CeO_2 afforded the lowest catalytic activity, yielding a pinene conversion of 11.4%, whereas the Cu−CeO_2 and Mn−CeO_2 nanocatalysts afforded similar conversions of 63.5 and 59.3%, respectively, under the H_2O_2-mediated hydroperoxidation reaction. The Fe−CeO_2 afforded the pinene conversion amount of 39.4%, while the Co−CeO_2 obtained 24.6% conversion. Interestingly, Ni−CeO_2 was the second-best-performing catalyst for the photooxidation reaction. It was, however, the least active under the H_2O_2 hydroperoxidation reaction conditions. This could be attributed to the fact that the NiO is considered a very poor redox catalyst for the conventional catalytic selective oxidation reactions compared to the highly redox-active Co, Cu, Fe, and Mn oxide counterparts. Thus, it has less ability to mediate oxidation reactions under conventional hydroperoxidation or molecular oxygen or air oxidation conditions. In contrast, the heterostructuring of NiO (p-type) with CeO_2 (n-type) created unique surface charge carriers and charge separation that effectively enhanced the photocatalytic performance. The major products in the hydroperoxidation reaction of pinene were determined to be verbenol and verbenone. These are the typical oxyfunctionalized products of the allylic oxidation reaction. Although the catalytic results for the heterostructured CeO_2 catalysts under hydroperoxidation conditions show that allylic C−H activation is favored, the photooxidation reaction of pinene showed high reactivity for epoxidation via unsaturated C−H activation, which resulted in the formation of pinene oxide as the main product. It is important to note that oxyfunctionalization reaction processes proceed differently. In the hydroperoxidation reaction, the reaction is initiated by the decomposition of the added "oxygen donor," H_2O_2, into the required reactive oxygen species (ROS) such as hydroxyl radicals ($^{\bullet}OH$) and hydroxyl ions (OH^-). On the other hand, for the photocatalytic oxidation reaction, the externally introduced molecular oxygen (O_2) is excited into reactive superoxide anions ($^{\bullet}O_2^-$) and peroxide ($^{\bullet}O_2^{-2}$). These excited $^{\bullet}O_2^-$ and $^{\bullet}O_2^{-2}$ species react with the available abstracted protons to create H_2O_2, which initiates the photocatalytic oxyfunctionalization reaction. On the basis of the obtained photocatalytic results, H-atom abstraction was more reactive at the unsaturated C−H bond site (i.e., epoxidation rather than allylic oxidation) under photocatalytic oxidation conditions.[50,51] An in-depth understanding of the catalytic behavior of these heterostructured CeO_2 catalysts in the oxidation of pinene under different activation conditions could provide significant insights into the further development of the optimum catalyst structure for selected oxidation reaction conditions and targeted organic molecule transformations. Although the current study does not provide a clear mechanism of the surface interactions of the reacting molecular species with the pinene oxidation substrate, it yields significant findings regarding the effects of the C−H activation conditions, which could perhaps be critical in controlling the product selectivity when both allylic and epoxidation C−H sites are highly reactive (Figure 12).

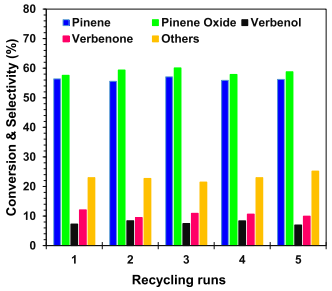

Figure 12. Recyclability performance tests of the Fe−CeO_2 catalyst in the pinene photooxidation reaction. Reaction conditions: pinene (10 mmol; 1.36 g), catalyst (0.10 g), acetonitrile (125 mL), T = 25 °C, and t = 3 h.

Recyclability of the Photocatalyst. The reusability of the catalyst with respect to stable conversion activity and product selectivity is very important for practical applications. Thus, we carried out recycling performance tests on the heterostructured Fe−CeO_2 nanocatalyst under visible-light irradiation conditions for pinene oxidation. The Fe−CeO_2

https://dx.doi.org/10.1021/acsomega.9b04396
ACS Omega 2020, 5, 9775−9788

nanocatalyst showed stable photocatalytic oxidation performance after being reused for five consecutive reaction cycles, although the conversion of pinene stabilized at 54−57% and the selectivity toward the key epoxidation product, pinene oxide, was maintained at 57−60% (Figure 9). Although these recyclability tests were limited to a few cycles, the results suggest that the catalyst has good stability, but further studies for long-term testing and optimization based on its structure−activity performance are required.

CONCLUSIONS

In summary, we have successfully synthesized heterostructured CeO_2 interfaced catalysts containing metal oxides (Cu, Co, Mn, Ni, and Fe) with uniformly distributed nanoparticle sizes and high surface areas. The heterostructured CeO_2-based nanocatalysts showed effective photocatalytic performance under visible-light irradiation for the oxidation of wood biomass-derived α-pinene to aroma oxygenated chemicals. Both Fe_2O_3−CeO_2 and NiO−CeO_2 photocatalysts afforded good pinene conversions of 71.3 and 53.1%, respectively, with corresponding pinene oxide selectivities of 57.3 and 58.2% after 5 h of reaction. The enhanced photocatalytic performance of the heterostructured CeO_2 catalysts compared to pristine CeO_2 is attributed to their enhanced visible-light absorption range, charge carriers, and efficient suppression of electron−hole recombination, facilitating the formation of reactive oxygen species for the oxyfunctionalization of pinene inert C−H. The Fe_2O_3−CeO_2 nanocatalyst was highly recyclable and did not show any significant loss of its photocatalytic activity. Further, the evaluation of the heterostructured CeO_2 catalysts under conventional chemocatalytic hydroperoxidation conditions revealed the formation of allylic oxidation products (i.e., verbenol and verbenone) with high selectivity compared to the pinene oxide epoxidation product under photo-irradiation conditions. Based on the characterization results including PL, UV−vis, XPS, and EPR, the enhanced electron/hole separations due to the contributions of the interactions of CeO_2 with the base metal oxide cocatalysts proved to be effective for improving the overall photocatalytic activity performance of the heterostructured CeO_2-based catalysts compared to neat CeO_2. Several induced structural modifications arising from defect oxygen vacancies, electronic interactions, and effective redox cycles exerted by the base metal oxide cocatalysts are proposed as the basis for the enhanced photocatalytic activity for the oxyfunctionalization for the pinene inert C−H to valuable aroma oxygenates.

EXPERIMENTAL SECTION

Materials and Reagents. All of the chemicals used in this work were of analytical grade and were purchased from Sigma−Aldrich (Germany) and Minema (South Africa). Cerium(III) nitrate hexahydrate ($Ce(NO_3)_3{\cdot}6H_2O$, 99.9%), copper(II) nitrate trihydrate ($Cu(NO_3)_2{\cdot}3H_2O$, 99.8%), cobalt(II) nitrate hexahydrate ($Co(NO_3)_2{\cdot}6H_2O$, 99.9%), nickel(II) nitrate hexahydrate ($Ni(NO_3)_2{\cdot}6H_2O$, 99.9%), manganese(II) nitrate tetrahydrate ($Mn(NO_3)_2{\cdot}4H_2O$, 98.0%), and iron(II) nitrate nonahydrate ($Fe(NO_3)_2{\cdot}9H_2O$, 99.9%) were used without further purification for the preparation of neat CeO_2 and heterostructured CeO_2-based metal oxide interfaced nanocatalysts. For the preparation of the interfaced nanocatalysts, ammonium hydroxide (NH_4OH, 28% NH_3 basis) was used as the precipitant, and polyvinyl pyrrolidone (PVP, M_w = 40 000) was used as the structure-directing agent. Ethanol (C_2H_5OH, EtOH) and deionized water (Millipore, Merck SA) were used as solvents.

Catalyst Preparation. The heterostructured ceria-composite nanocatalysts were prepared by sol−gel synthesis. First, solution A was prepared by dissolving 24 mmol $Ce(NO_3)_3{\cdot}6H_2O$ in 50 mL of deionized water with continuous stirring. Solution B was prepared by dissolving an appropriate amount of the base metal precursor salts ($Cu(NO_3)_2{\cdot}3H_2O$, $Co(NO_3)_2{\cdot}6H_2O$, $Ni(NO_3)_2{\cdot}6H_2O$, $Mn(NO_3)_2{\cdot}4H_2O$, or $Fe(NO_3)_2{\cdot}9H_2O$) in 150 mL of EtOH with magnetic stirring to give 20 wt % loading in CeO_2. Then, solution A was added to solution B dropwise with constant magnetic stirring. The pH of the respective mixtures was adjusted to 10 using 28% aq. NH_4OH. The solution was maintained under reflux with continuous stirring for a further 20 h at 100 °C. Thereafter, the solution was allowed to cool before the catalyst slurries were filtered and washed with acetone and methanol sequentially using centrifugation. The samples were then dried at 100 °C for 24 h and subsequently calcined in air at 3 °C/min to 500 °C and then held at that temperature for 2 h. The pristine CeO_2 NPs were synthesized by dissolving 24 mmol $Ce(NO_3)_3$ in 50 mL of deionized water with continuous stirring, followed by the addition of 150 mL of EtOH. The reaction solution pH was adjusted to 10 using NH_4OH, followed by continuous stirring under reflux at 100 °C for 24 h. The obtained CeO_2 NPs were filtered, dried, and calcined in a similar manner to the heterostructure CeO_2-based metal oxide interfaces.

Catalyst Characterization. The crystalline structures of the synthesized heterostructured CeO_2-based nanocatalysts were determined by powder X-ray diffractometry (XRD, PANalytical X'PERT-PRO diffractometer, the Netherlands). The diffractometer was operated at 45 kV and 40 mA. The diffraction peaks were indexed by comparison with the Powder Data File database (International Centre of Diffraction Data). The surface areas and pore distributions of the samples were analyzed on a Micromeritics instrument (Tri-Star III 3020) using nitrogen physisorption at −196 °C and analyzed using the Brunauer−Emmett−Teller (BET) and Barret−Joyner−Halenda (BJH) isotherms. The morphologies of the prepared ceria samples were characterized by scanning electron microscopy (SEM) on a Zeiss-Auriga focused-ion-beam (FIB) scanning electron microscope operated at 3 keV. The light absorption edges of the samples were characterized by ultraviolet−visible−near-infrared spectroscopy (UV−vis−NIR) from 200 to 1200 nm using a Perkin Elmer Lambda 750 UV−vis−NIR spectrometer. The charge recombination of the heterostructure CeO_2-based metal oxide interface nanocatalysts was determined by photoluminescence (PL) spectroscopy using a HORIBA Jobin Yvon Nanolog spectrofluorometer at an excitation wavelength of 325 nm. The emission peaks were investigated at wavelengths ranging from 400 to 800 nm. The elemental, electronic binding energy, and oxidation states were obtained by employing X-ray photoelectron spectroscopy (XPS) using a Thermo Fischer scientific ESCAlab 250Xi spectroscope that employed monochromatic Al Kα as the excitation source. The microwave absorption spectra were analyzed using a JEOL X-band electron paramagnetic resonance (EPR) spectrometer (JES FA 200) at ambient temperature.

Photocatalytic Activity Testing. The photocatalytic oxidation of pinene was carried out using a water-cooled double-walled photoreactor (150 mL volume capacity) fitted

https://dx.doi.org/10.1021/acsomega.9b04396
ACS Omega 2020, 5, 9775−9788

with a 125 W medium-mercury lamp (Photochemical Reactors Ltd., England). In each experiment, 10 mmol (1.36 g) pinene and 0.10 g of the catalyst were dispersed in 125 mL of acetonitrile. The lamp was turned on, the reaction was allowed to proceed for 5 h at 25 °C, and O_2 was made to flow continuously through the reaction suspension for all experiments measured at 25 mL/min flow rate. After 5 h, the reaction suspension was centrifuged to remove the nanocatalyst particles for the analysis of the pinene oxygenates by gas chromatography (GC) using a Supelco SPB-20 column (30 m × 0.25 mm i.d. × 0.25 mm) on an Agilent 7890A gas chromatograph fitted with a flame ionization detector (FID). The GC analysis program was as follows: FID temperature, 300 °C; injector temperature, 250 °C; and oven column temperature, 50 °C (3 min). This was followed by ramping to 200 °C at 10 °C/min. The products were identified by comparing their retention times to those of authentic samples and others by GC-mass spectrometry (MS). Nitrobenzene was used as an internal standard with methanol as the solvent for the GC quantitative analysis of the different oxidation products.

■ ASSOCIATED CONTENT

Supporting Information

The Supporting Information is available free of charge at https://pubs.acs.org/doi/10.1021/acsomega.9b04396.

Data of XRD, PL, and XPS results (PDF)

■ AUTHOR INFORMATION

Corresponding Authors

Peter R. Makgwane − *Centre for Nanostructures and Advanced Materials, Council for Scientific and Industrial Research (CSIR), Pretoria 0001, South Africa; Department of Chemistry, University of the Western Cape, Bellville 7535, South Africa;* orcid.org/0000-0002-0109-4665; Email: pmakgwane@csir.co.za, makgwane.peter@gmail.com

Suprakas Sinha Ray − *Department of Chemical Sciences, University of Johannesburg, 2028 Johannesburg, South Africa; Centre for Nanostructures and Advanced Materials, Council for Scientific and Industrial Research (CSIR), Pretoria 0001, South Africa;* orcid.org/0000-0002-0007-2595; Email: rsuprakas@csir.co.za

Author

Mlungisi A. Mavuso − *Department of Chemical Sciences, University of Johannesburg, 2028 Johannesburg, South Africa*

Complete contact information is available at: https://pubs.acs.org/10.1021/acsomega.9b04396

Notes

The authors declare no competing financial interest.

■ ACKNOWLEDGMENTS

This research was funded by CSIR Thematic SRP for the development of green and renewable chemicals (Grant No. T18#2016-2019) and a CSIR parliamentary grant (No. HGER46s-2018-2019). M.A.M. thanks the CSIR-HCD and NRF for scholarships to enable Ph.D. study.

■ REFERENCES

(1) Golets, M.; Ajaikumar, S.; Mikkola, J.-P. Catalytic upgrading of extractives to chemicals: Monoterpenes to "EXICALS". *Chem. Rev.* **2015**, *115*, 3141−3169.

(2) Corma, A.; Iborra, S.; Velty, A. Chemical routes for the transformation of biomass into chemicals. *Catal. Rev.* **2007**, *107*, 2411−2502.

(3) Cao, Y.; Li, Y.; Yu, H.; Peng, F.; Wang, H. Aerobic oxidation of α-pinene catalyzed by carbon nanotubes. *Catal. Sci. Technol.* **2015**, *5*, 3935−3944.

(4) Ajaikumar, S.; Ahlkvist, J.; Larsson, W.; Shchukarev, A.; Leino, A. R.; Kordas, K.; Mikkola, J.-P. Oxidation of α-pinene over gold containing bimetallic nanoparticles supported on reducible TiO_2 by deposition-precipitation method. *Appl. Catal., A* **2011**, *392*, 11−18.

(5) Chen, L.; Tang, J.; Song, L.-N.; Chen, P.; He, J.; Au, C.-T.; Yin, S.-F. Heterogeneous photocatalysis for selective oxidation of alcohols and hydrocarbons. *Appl. Catal., B* **2019**, *242*, 379−388.

(6) Colmenares, J. C.; Luque, R. Heterogeneous photocatalytic nanomaterials: prospects and challenges in selective transformations of biomass-derived compounds. *Chem. Soc. Rev.* **2014**, *43*, 765−778.

(7) Zhang, H.; Wu, Q.; Guo, C.; Wu, Y.; Wu, T. Photocatalytic selective oxidation of 5-hydroxymethylfurfural to 2,5-diformylfuran over Nb_2O_5 under visible light. *ACS Sustainable Chem. Eng.* **2017**, *5*, 3517−3523.

(8) Li, Y.; Sun, Q.; Kong, M.; Shi, W.; Huang, J.; Tang, J.; Zhao, X. Coupling oxygen ion conduction to photocatalysis in mesoporous nanorod-like ceria significantly improves photocatalytic efficiency. *J. Phys. Chem. C* **2011**, *115*, 14050−14057.

(9) Kou, J.; Lu, C.; Wang, J.; Chen, Y.; Xu, Z.; Varma, R. S. Selectivity enhancement in heterogeneous photocatalytic transformations. *Chem. Rev.* **2017**, *117*, 1445−1514.

(10) Zhang, X.; Chen, Y. L.; Liu, R.-S.; Tsai, D. P. Plasmonic photocatalysis. *Rep. Prog. Phys.* **2013**, *76*, No. 046401.

(11) Lang, X.; Ji, H.; Chen, C.; Ma, W.; Zhao, J. Selective formation of imines by aerobic photocatalytic oxidation of amines on TiO_2. *Angew. Chem., Int. Ed.* **2011**, *50*, 3934−3937.

(12) Khan, M. M.; Ansari, S. A.; Ansari, M. O.; Min, B. K.; Lee, J.; Cho, M. H. Biogenic fabrication of Au@CeO_2 nanocomposite with enhanced visible light activity. *J. Phys. Chem. C* **2014**, *118*, 9477−9484.

(13) Yue, L.; Zhang, X.-M. Structural characterization and photocatalytic behaviors of doped CeO_2 nanoparticles. *J. Alloys Compd.* **2009**, *475*, 702−705.

(14) Zhang, M.; Chen, C.; Ma, W.; Zhao, J. Visible-light-induced aerobic oxidation of alcohols in a coupled photocatalytic system of dye-sensitized TiO_2 and TEMPO. *Angew. Chem., Int. Ed.* **2008**, *47*, 9730−9733.

(15) Zhang, Z.; Luo, Z.; Yang, Z.; Zhang, S.; Zhang, Y.; Zhou, Y.; Wang, X.; Fu, X. Band-gap tuning of N-doped TiO_2 photocatalysts for visible-light-driven selective oxidation of alcohols to aldehydes in water. *RSC Adv.* **2013**, *3*, 7215−7218.

(16) Hu, S.; Zhou, F.; Wang, L.; Zhang, J. Preparation of Cu_2O/CeO_2 heterojunction photocatalyst for the degradation of acid orange 7 under visible light irradiation. *Catal. Commun.* **2011**, *12*, 794−797.

(17) Wetchakun, N.; Chaiwichain, S.; Inceesungvorn, B.; Pingmuang, K.; Phanichphant, S.; Minett, A. I.; Chen, J. $BiVO_4$/CeO_2 nanocomposites with high visible-light-induced photocatalytic activity. *ACS Appl. Mater. Interfaces* **2012**, *4*, 3718−3723.

(18) Ji, P.; Zhang, J.; Chen, F.; Anpo, M. Ordered mesoporous CeO_2 synthesized by nanocasting from cubic Ia3d mesoporous MCM-48 silica: Formation, characterization and photocatalytic activity. *J. Phys. Chem. C* **2008**, *112*, 17809−17813.

(19) Zou, W.; Shao, Y.; Pua, Y.; Luo, Y.; Sun, J.; Ma, K.; Tang, C.; Gao, F.; Dong, L. Enhanced visible light photocatalytic hydrogen evolution via cubic CeO_2 hybridized g-C_3N_4 composite. *Appl. Catal., B* **2017**, *218*, 51−59.

(20) Arul, N. S.; Mangalaraj, D.; Ramachandran, R.; Grace, A. N.; Han, J. I. Fabrication of CeO_2/Fe_2O_3 composite nanospindles for

enhanced visible light driven photocatalyst and supercapacitor electrode. *J. Mater. Chem. A* **2015**, *3*, 15248−15258.
(21) Cui, Z.; Wang, W.; Zhao, C.; Chen, C.; Han, M.; Wang, G.; Zhang, Y.; Zhang, H.; Zhao, H. Spontaneous redox approach to the self-assembly synthesis of Au/CeO_2 plasmonic photocatalysts with rich oxygen vacancies for selective photocatalytic conversion of alcohols. *ACS Appl. Mater. Interfaces* **2018**, *10*, 31394−31403.
(22) Zhang, N.; Liu, S.; Fu, X.; Xu, Y.-J. A simple strategy for fabrication of "plum-pudding" type Pd@CeO_2 semiconductor nanocomposite as a visible-light-driven photocatalyst for selective oxidation. *J. Phys. Chem. C* **2011**, *115*, 22901−22909.
(23) Liu, Y.; Jiang, G.; Li, L.; Chen, H.; Huang, Q.; Du, X.; Tong, Z. Electrospun CeO_2/Ag@carbon nanofiber hybrids for selective oxidation of alcohols. *Powder Technol.* **2017**, *305*, 597−601.
(24) Zhang, N.; Fu, X.; Xu, Y.-J. A facile and green approach to synthesize Pt@CeO_2 nanocomposite with tunable core-shell and yolk-shell structure and its application as a visible light photocatalyst. *J. Mater. Chem.* **2011**, *21*, 8152−8158.
(25) Tana, M.; Zhang, J.; Li, H.; Li, Y.; Li, W. Shen, Morphology-dependent redox and catalytic properties of CeO_2 nanostructures: nanowires, nanorods and nanoparticles. *Catal. Today* **2009**, *148*, 179−183.
(26) Wu, Z.; Li, M.; Overbury, S. H. On the structure dependence of CO oxidation over CeO_2 nanocrystals with well-defined surface planes. *J. Catal.* **2012**, *285*, 61−73.
(27) Vaseem, M.; Umar, A.; Hahn, Y. B.; Kim, D. H.; Lee, K. S.; Jang, J. S.; Lee, J. S. Flower-shaped CuO nanostructures: Structural, photocatalytic and XANES studies. *Catal. Commun.* **2008**, *10*, 11−16.
(28) Wang, Y.; Yang, C.-M.; Schmidt, W.; Spliethoff, B.; Bill, E.; Schüth, F. Weakly ferromagnetic ordered mesoporous Co_3O_4 synthesized by nanocasting from vinyl-functionalized cubic Ia3d mesoporous silica. *Adv. Mater.* **2005**, *17*, 53−56.
(29) Mahmoud, W. E.; Al-Hazmi, F.; Al-Noaiser, F.; Al-Ghamdi, A. A.; Bronstein, L. M. A facile method to syntheses monodisperse γ-Fe_2O_3 nanocubes with high magnetic anisotropy density. *Superlattices Microstruct.* **2014**, *68*, 1−5.
(30) Khatri, A.; Rana, P. S. Visible light photocatalysis of methylene blue using cobalt substituted cubic NiO nanoparticles. *Bull. Mater. Sci.* **2019**, *42*, No. 141.
(31) Giannakoudakis, D. A.; Nair, V.; Khan, A.; Deliyanni, E. A.; Colmenares, J. C.; Triantafyllidis, K. S. Additive-free photo-assisted selective partial oxidation at ambient conditions of 5-hydroxymethylfurfural by manganese (IV) oxide nanorods. *Appl. Catal., B* **2019**, *256*, No. 117803.
(32) Phoka, S.; Laokul, P.; Swatsitang, E.; Promarak, V.; Seraphin, S.; Maensiri, S. Synthesis, structural and optical properties of CeO_2 nanoparticles synthesized by a simple polyvinyl pyrrolidone (PVP) solution route. *Mater. Chem. Phys.* **2009**, *115*, 423−428.
(33) Liu, B.; Liu, B.; Li, Q.; Li, Z.; Liu, R.; Zou, X.; Wu, W.; Cui, W.; liu, Z.; Li, D.; Zou, B.; Cui, T.; Zou, G. Solvothermal synthesis of monodisperse self-assembly CeO_2 nanospheres and their enhanced blue-shifting in ultraviolet absorption. *J. Alloys Compd.* **2010**, *503*, 519−524.
(34) Wang, L.; Meng, F.; Li, K.; Lu, F. Characterization and optical properties of pole-like nano-CeO_2 synthesized by a facile hydrothermal method. *Appl. Surf. Sci.* **2013**, *286*, 269−274.
(35) Gnanam, S.; Rajendran, V. Influence of various surfactants on size, morphology and optical properties of CeO_2 nanostructures via facile hydrothermal route. *J. Nanopart.* **2013**, No. 839391.
(36) Sang, Y.; Liu, H.; Umar, A. Photocatalysis from UV/Vis to near-infrared light: towards full solar-light spectrum activity. *ChemCatChem* **2015**, *7*, 559−573.
(37) Zang, C.; Zhang, X.; Hu, S.; Chen, F. The role of exposed facets in the Fenton-like reactivity of CeO_2 nanocrystal to the Orange II. *Appl. Catal., B* **2017**, *216*, 106−113.
(38) Renuka, N. K. Structural characteristics of quantum-size ceria nano particles synthesized via simple ammonia precipitation. *J. Alloys Compd.* **2012**, *513*, 230−235.
(39) Aškrabić, S.; Dohčević-Mitrović, Z. D.; Araujo, V. D.; Ionita, G.; de Lima, M. M., Jr.; Cantarero, A. F-centre luminescence in nanocrystalline CeO_2. *J. Phys. D: Appl. Phys.* **2013**, *46*, No. 495306.
(40) Wang, F.; Buchel, R.; Savitsky, A.; Zalibera, M.; Widmann, D.; Pratsinis, S. E.; Lubitz, W.; Schuth, F. In situ EPR study of the redox properties of CuO-CeO_2 catalysts for preferential CO oxidation (PROX). *ACS Catal.* **2016**, *6*, 3520−3530.
(41) Rakhmatullin, R. M.; Pavlov, V. V.; Semashko, V. V. EPR study of nanocrystalline CeO_2 exhibiting ferromagnetism at room temperature. *Phys. Status Solidi B* **2016**, *253*, 499−503.
(42) Abi-Aad, E.; Bennani, A.; Bonnelle, J.-P.; Aboukaïs, A. Transition-metal ion dimers formed in CeO_2: An EPR study. *J. Chem. Soc., Faraday Trans.* **1995**, *91*, 99−104.
(43) Neuenschwander, U.; Guignard, F.; Hermans, I. Mechanism of the aerobic oxidation of α-pinene. *ChemSusChem* **2010**, *3*, 75−84.
(44) Marschall, R. Semiconductor composites: strategies for enhancing charge carrier separation to improve photocatalytic activity. *Adv. Funct. Mater.* **2014**, *24*, 2421−2440.
(45) Rawool, S. A.; Pai, M. R.; Banerjee, A. M.; Arya, A.; Ningthoujam, R. S.; Tewari, R.; Rao, R.; Chalke, B.; Ayyub, P.; Tripathi, A. K.; Bharadwaj, S. R. *pn* Heterojunctions in NiO:TiO_2 composites with type-II alignment assisting sunlight driven photocatalytic H_2 generation. *Appl. Catal., B* **2018**, *221*, 443−458.
(46) Emin, S.; Abdi, F. F.; Fanetti, M.; Peng, W.; Smith, W.; Sivula, K.; Dam, B.; Valant, M. A novel approach for the preparation of textured CuO thin films from electrodeposited CuCl and CuBr. *J. Electroanal. Chem.* **2014**, *717−718*, 243−249.
(47) Ren, X.; Gao, P.; Kong, X.; Jiang, R.; Yang, P.; Chen, Y.; Chi, Q.; Li, B. NiO/Ni/TiO_2 nanocables with Schottky/p-n heterojunctions and the improved photocatalytic performance in water splitting under visible light. *J. Colloid Interface Sci.* **2018**, *530*, 1−8.
(48) Liu, J.; Li, Y.; Ke, J.; Wang, S.; Wang, L.; Xiao, H. Black NiO-TiO_2 nanorods for solar photocatalysis: Recognition of electronic structure and reaction mechanism. *Appl. Catal., B* **2018**, *224*, 705−714.
(49) Rawool, S. A.; Pai, M. R.; Banerjee, A. M.; Aryab, A.; Ningthoujam, R. S.; Tewari, R.; Rao, R.; Chalke, B.; Ayyub, P.; Tripathi, A. K.; Bharadwaj, S. R. PN heterojunctions in NiO:TiO_2 composites with type-II band alignment assisting sunlight driven photocatalytic H_2 generation. *Appl. Catal., B* **2018**, *221*, 443−458.
(50) Maldonado, A. C. M.; Winkler, E. L.; Raineri, M.; Córdova, A. T.; Rodríguez, L. M.; Troiani, H. E.; Pisciotti, M. L. M.; Mansilla, M. V.; Tobia, D.; Nadal, M. S.; Torres, T. E.; De Biasi, E.; Ramos, C. A.; Goya, G. F.; Zysler, R. D.; Lima, E., Jr. Free-Radical Formation by the Peroxidase-Like Catalytic Activity of MFe_2O_4 (M = Fe, Ni, and Mn) nanoparticles. *J. Phys. Chem. C* **2019**, *123*, 20617−20627.
(51) Hallett-Tapley, G. L.; Silvero, M. J.; González-Béjar, M.; Grenier, M.; Netto-Ferreira, J. C.; Scaiano, J. C. Plasmon-mediated catalytic oxidation of sec-phenethyl and benzyl alcohols. *J. Phys. Chem. C* **2011**, *115*, 10784−10790.

https://dx.doi.org/10.1021/acsomega.9b04396
ACS Omega 2020, 5, 9775−9788